



Light assisted CO₂ reduction with methane over group VIII metals: Universality of metal localized surface plasmon resonance in reactant activation



Huimin Liu^a, Thang Duy Dao^{a,c}, Lequan Liu^{b,d,*}, Xianguang Meng^a, Tadaaki Nagao^{a,c}, Jinhua Ye^{a,b,d,*}

^a International Center for Materials Nanoarchitectonics (WPI-MANA), National Institute for Materials Science (NIMS), 1-1 Namiki, Tsukuba, Ibaraki 305-0044, Japan

^b TU-NIMS International Collaboration Laboratory, School of Materials Science and Engineering, Tianjin University, 92 Weijin Road, Nankai District, Tianjin 300072, China

^c CREST, Japan Science and Technology Agency (JST), 4-1-8 Honcho, Kawaguchi, Saitama 332-0012, Japan

^d Collaborative Innovation Center of Chemical Science and Engineering (Tianjin), Tianjin 300072, China

ARTICLE INFO

Article history:

Received 16 January 2017

Received in revised form 20 February 2017

Accepted 28 February 2017

Available online 6 March 2017

Keywords:

Localized surface plasmon resonance

Carbon dioxide

Light assistance

Group VIII metal

Photocatalysis

ABSTRACT

Photo-catalytically reducing the greenhouse gas CO₂ into valuable compounds is beneficial for environmental protection. In this study, a recently developed novel CO₂ photoreduction approach, light assisted thermal-driven CO₂ reforming with CH₄ into syngas (DRM), is adopted as the target reaction, with group VIII metals, especially Ni/Al₂O₃, as the probe catalysts. With light introduction, the activities of Ni/Al₂O₃ nearly linearly increased and the increments were in highly correspondence to the intensity of the electromagnetic field induced by two adjacent Ni particles, together with the wavelength-dependent performances over 10Ni/Al₂O₃, it indicated it was Ni localized surface plasmon resonance (LSPR) that improved the performances. The LSPR enhanced catalytic performance could also be observed over other group VIII metals, such as Rh- and Fe-based catalysts, and the universality of reactant activation by metal LSPR could be expected. This study firstly revealed that not merely limited to IB metals, group VIII metals could also be adopted as plasmonic promoters and enhance the activity of a catalyst with light irradiation.

© 2017 Elsevier B.V. All rights reserved.

1. Introduction

Photo-catalytically reducing CO₂ with CH₄ into syngas (DRM) is a promising approach for both decreasing the concentration of greenhouse gas CO₂ in the atmospheric air [1–8] and converting the abundant solar energy to chemical energy [9,10], whereas high temperature (800–1000 °C) was required for DRM industrialization [11,12]. Reducing the reaction temperature or improving the activity of a catalyst in DRM at low temperatures has become the hot spot of researches recently. The activities of catalysts could be enhanced by introducing solar energy into a thermal-driven reaction system provided that materials of strong localized surface plasmon resonance (LSPR) were adopted as plasmonic promoter [13–17]. However, IB metals, which possess strong LSPR properties in visible

light region, were generally expensive and inactive for thermal-driven CO₂ reduction reactions [18,19], therefore, it is urgent and significant to search for efficient and economical plasmonic promoters.

As is known, the active components for thermal-driven DRM reaction were mainly group VIII metals [20–23]. Meanwhile, group VIII metals have also been adopted as promoters with light irradiation in the optical range recently [24–27]. To this aspect, the activities of group VIII metal-based catalysts are expected to be enhanced and become more economical with solar light being introduced to the thermal-driven reaction system.

Among the many group VIII metals, Ni, one of the most substantial metals in the earth [28,29], was widely studied as an active component in the thermal-driven DRM due to its low price and fairish catalytic activity [20–23]. On the other hand, there was rare study adopting Ni as optical promoter, and exploring the optical properties of Ni is of great importance to the area of photocatalysis. What's more, over Ni-based catalysts, the elementary reaction between the adsorbed CH_x^{*} (the intermediate of CH₄ cleavage) and

* Corresponding authors at: TU-NIMS International Collaboration Laboratory, School of Materials Science and Engineering, Tianjin University, 92 Weijin Road, Nankai District, Tianjin 300072, China.

E-mail addresses: lequan.liu@tju.edu.cn (L. Liu), Jinhua.YE@nims.go.jp (J. Ye).

O^* species (generated by CO_2 dissociation) was regarded to be the rate determining step for Ni/Al_2O_3 catalyst [30–32], which might be facilitated by introducing extra light to the reaction system and give us an opportunity to investigate the reasons for the enhanced catalytic activities. Herein, Ni/Al_2O_3 catalysts of varied Ni loadings, with Ni serving both as the active catalytic component and the optical promoter, were prepared by wetness impregnation method and the catalytic activities of the catalysts were evaluated with the aim to study the phenomena of reactant activation by group VIII metals.

2. Experimental section

2.1. Catalyst preparation

Commercial $Ni(NO_3)_2 \cdot 6H_2O$, $RhCl_3 \cdot 3H_2O$, $Fe(NO_3)_3 \cdot 9H_2O$, K_2PdCl_6 , H_2PtCl_4 , SiO_2 and Al_2O_3 were purchased from Wako pure chemical industries Ltd and used as received.

Preparation of Ni/Al_2O_3 : Ni/Al_2O_3 catalysts were prepared by wetness impregnation method. A portion of Al_2O_3 support was added into the $Ni(NO_3)_2 \cdot 6H_2O$ aqueous solution with a fixed amount of $Ni(NO_3)_2 \cdot 6H_2O$, stirred for 10 h and then evaporated, dried and calcined at 550 °C for 5 h. The obtained samples were named as $xNiO/Al_2O_3$, where x represented the theoretical Ni loadings. After reducing in H_2/Ar at 900 °C for 1 h, the samples were transformed into the reduced catalysts xNi/Al_2O_3 .

Additionally, Ni/SiO_2 , Rh/SiO_2 , Fe/SiO_2 , Pd/Al_2O_3 and Pt/Al_2O_3 were also prepared by wetness impregnation method, and the procedures were similar with that of Ni/Al_2O_3 .

2.2. Material characterization

The crystalline structures of the support Al_2O_3 and Ni-based catalysts were analyzed by X-ray diffraction (XRD) method, on an X-Pert diffractometer equipped with graphite monochromatized $Cu-K\alpha$ radiation. The specific surface areas were determined with a surface area analyzer (BEL Sorp-II mini, BEL Japan Co., Japan) by the Brunauer-Emmett-Teller (BET) method. The morphology and the sizes of Ni particles were observed on transmission electron microscope JEM-2100 (JEOL Ltd, Japan). The diffuse reflection spectra of the catalysts were measured by UV-vis spectrophotometer (UV-2600, SHIMADZU Co., Japan) from 200 nm to 1400 nm. The contents of Ni on the catalysts were analyzed by inductively coupled plasma optical emission spectrometry (ICP-OES, SPS3520UV-DD, SII nano technology Inc., Japan). The existences of Ni on the catalysts were identified by X-ray photoelectron spectroscopy (XPS, PHI Quantera SXM, ULVAC-PHI Inc., Japan).

2.3. Catalyst evaluation

DRM reaction was conducted in a fixed-bed reactor under atmospheric pressure. A 0.050 g portion of catalyst without dilution was packed uniformly in the alumina cell. Both TC-1000 temperature controller (Jacso) and LA-251Xe lamp (Hayashi) with HA30 filter were employed to provide the energy input. CH_4 and CO_2 with the molar ratio of 1/1 were introduced into the reactor at a total flowrate of 20.0 mL/min (STP). The effluent gas were analyzed off-line by injection method on two separate gas chromatography (GC). H_2 was analyzed on GC-8A, Shimadzu Co., Japan, while CO , CO_2 and CH_4 were analyzed on GC-14B, Shimadzu Co., Japan. The flowrate of the effluent gas was measured with a flowmeter.

2.4. Theoretical simulation of Ni LSPR spectrum

The plasmonic absorption spectrum of Ni particles on $10Ni/Al_2O_3$ was simulated by Mie theory, and an average diameter of 10 nm was used for simulation, which was obtained from TEM

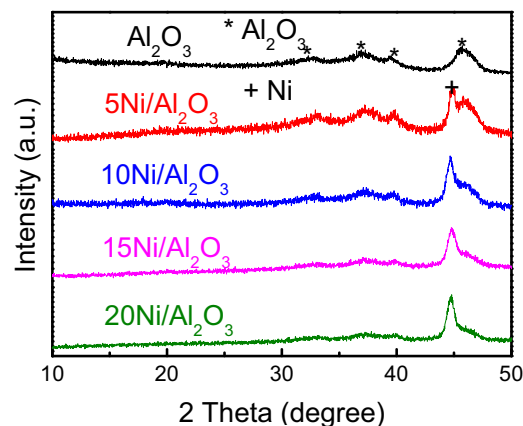


Fig. 1. XRD patterns of Al_2O_3 and Ni/Al_2O_3 catalysts.

and XRD analysis. The dielectric constant for Ni was taken from the report by Johnson and Christy [33], and the actual reaction atmosphere that Ni particles were mainly enclosed by gaseous reactant CO_2 and CH_4 was also taken into consideration.

2.5. Electromagnetic field simulation

The electromagnetic fields distributed around plasmonic catalysts were calculated using finite-difference time-domain (FDTD) methods (FullWAVE, Synopsys' RSoft). The dielectric functions of Ni and Al_2O_3 were taken from the literature [34]. The model of the plasmonic catalysts was performed in a cad layout (RSoft CAD), with both the average Ni sizes and the Ni-Ni distances being taken into consideration. The excitation electromagnetic field propagated along Z axis and oscillated along X axis. The simulation domain was chosen with a grid size of 0.2 nm, and in a conjunction sequentially with a perfectly matched layer boundary condition. The amplitudes of the incident fields were normalized to 1.

3. Results and discussion

3.1. Physicochemical properties of the Ni/Al_2O_3 catalysts

The crystalline phases of the Ni/Al_2O_3 catalysts were characterized by XRD (Fig. 1). From the XRD profiles of Ni/Al_2O_3 catalysts, except the diffraction peaks assigned to support $\gamma-Al_2O_3$, the peak centered at 44.7° attributed to Ni could also be observed, together with the XPS analysis in Fig. S1 it suggested that Ni was successfully loaded on support Al_2O_3 . The actual Ni loadings analysed by ICP-OES method were close to the theoretical values (Table 1). The loading of Ni influenced little on the specific surface areas and pore size distributions of the catalysts (Fig. S2 and Table 1). The sizes of Ni particles over these catalysts were calculated via Scherrer equation through the Ni diffraction peak at 44.7°, and listed in Table 1. Clearly, the size of Ni particles increased gradually with Ni loadings, from 9.7 nm over $5Ni/Al_2O_3$ to 16.5 nm over $20Ni/Al_2O_3$, which were consistent with those obtained from TEM images (Fig. S3 and Table 1). The formation of relatively large Ni particles was probably due to the limited surface area of Al_2O_3 (Table 1), the strong interactions between Ni and Al_2O_3 (Fig. S4) and the high NiO reduction temperatures (Fig. S5). The dispersion of Ni particles on these catalysts was obtained by H_2 -TPR-TPD method (Figs. S5 and S6) [35] and shown in Table 1. $5Ni/Al_2O_3$ and $10Ni/Al_2O_3$ possessed high and comparable Ni dispersions (10.4%–10.8%), whereas the degree of Ni dispersion was reduced with the further increase of Ni loadings (7.9% on $15Ni/Al_2O_3$ and 3.7% on $20Ni/Al_2O_3$). The amount of Ni active sites, which played the crucial role in determining the

Table 1

Physicochemical properties of support Al_2O_3 and $\text{Ni}/\text{Al}_2\text{O}_3$ catalysts.

Samples	$S_{\text{BET}} (\text{m}^2 \text{g}^{-1})^{\text{a}}$	Ni loading (wt.%) ^b	Ni size (nm) ^c	Ni size (nm) ^d	Ni–Ni distance (nm) ^d	Ni dispersion (%) ^e	Active Ni sites (wt.%) ^f
Al_2O_3	168	–	–	–	–	–	–
5Ni/ Al_2O_3	163	4.8	9.7	9.5	9.0	10.8	0.52
10Ni/ Al_2O_3	154	9.2	10.5	10.1	6.5	10.4	0.96
15Ni/ Al_2O_3	160	13.4	12.8	13.4	9.2	7.9	1.06
20Ni/ Al_2O_3	140	17.3	16.5	17.2	12.7	3.7	0.64

^a Obtained by N_2 adsorption–desorption method through Brunauer–Emmett–Teller (BET) equation.

^b Analyzed by ICP-OES method.

^c Calculated via Scherrer equation through the Ni diffraction peak at 44.7° .

^d Obtained from the TEM images.

^e Calculated from the H_2 -TPR-TPD profiles in Figs. S5 and S6.

^f The product of Ni loading and Ni dispersion.

catalytic activity of a catalyst in thermal-driven reactions [36], were calculated and displayed in Table 1. Catalysts with proper Ni loading contents possessed the highest amount of Ni active sites (0.96 wt.% on 10Ni/ Al_2O_3 and 1.06 wt.% on 15Ni/ Al_2O_3), whereas low or excessive Ni loadings were unfavourable for providing more active sites owing to the low Ni contents (0.52 wt.% on 5Ni/ Al_2O_3) or low Ni dispersions (0.64 wt.% on 20Ni/ Al_2O_3).

3.2. Catalytic performances of the $\text{Ni}/\text{Al}_2\text{O}_3$ catalysts

The performances of the $\text{Ni}/\text{Al}_2\text{O}_3$ catalysts with various Ni loadings were evaluated in DRM with light irradiation ($300 \text{ nm} < \lambda < 800 \text{ nm}$), shown in Figs. 2 and S7–S10. Clearly, without light irradiation, each of the $\text{Ni}/\text{Al}_2\text{O}_3$ catalyst exhibited low catalytic performances (CH_4 conversions were in the range of $14.6\text{--}38.5 \mu\text{mol g}^{-1} \text{min}^{-1}$, and CO_2 conversions were in the range of $15.9\text{--}46.9 \mu\text{mol g}^{-1} \text{min}^{-1}$), and the highest catalytic activity was obtained over 15Ni/ Al_2O_3 , which was proportional to the available Ni active sites (Fig. S11). On the contrary, it's interesting to note that, after the introduction of light, the catalytic performances were nearly linearly enhanced with the increase of light intensity, and the enhancement could even be observed at the light intensity as high as 1.07 W cm^{-2} , which implied that Ni particles were stable and not severely aggregated under the evaluation condition [20–23]. Additionally, the slopes for the increment varied with Ni loadings (Fig. 2) in the order of $10\text{Ni}/\text{Al}_2\text{O}_3 > 5\text{Ni}/\text{Al}_2\text{O}_3 \approx 15\text{Ni}/\text{Al}_2\text{O}_3 > 20\text{Ni}/\text{Al}_2\text{O}_3$. For all the cases, CO_2 conversions were slightly higher than CH_4 conversions due to the side reaction between CO_2 and product H_2 (reverse water gas shift reaction) [37–39]. What's more, the selectivities to H_2 and CO , and the mass balances were all close to 100%, which lead to the analogous increase trend of H_2 and CO yields to those of CH_4 and CO_2 conversions (Fig. 2).

3.3. Reasons for the enhanced catalytic performances of the $\text{Ni}/\text{Al}_2\text{O}_3$ catalysts with light irradiation

To make clear the reason for the enhanced performance of $\text{Ni}/\text{Al}_2\text{O}_3$ in DRM with light irradiation, catalyst-bed temperature was carefully monitored. It is found that, without extra heat supply, temperature increases were indeed observed with light irradiation (Fig. S12). However, no temperature fluctuation was detected in the light assisted thermal-driven catalytic system and the reaction temperature remained stable at 550°C (Fig. S13), the reason for the stable temperature control was that the energy from heater was less supplied and compensated to the system in the case of more intensive light irradiation. Together with the non-enhanced catalytic performances of Pd and Pt-based catalysts with light irradiation (Figs. S14 and S15) and the differences in activity increment slopes of the $\text{Ni}/\text{Al}_2\text{O}_3$ catalysts (Figs. 2 and S12), it could be concluded that the reaction temperature was well controlled in the light assisted thermal-driven reaction system, and it was not photo-

induced temperature increase that enhanced the performances of $\text{Ni}/\text{Al}_2\text{O}_3$ catalysts.

From the UV-vis spectra in Figs. 3a and S16 it could be seen that, over the $\text{Ni}/\text{Al}_2\text{O}_3$ catalysts, the absorption edge assigned to Al_2O_3 was not observed (Figs. S17 and S18), which was probably due to the severe impediment of light transmission by the black Ni particles dispersed on the outmost surface of Al_2O_3 (Fig. S3). Meanwhile, a broad peak centered at about 420 nm was observed, which was attributed to the typical absorption of metallic Ni [24–27]. The peak heavily tailed to the infrared region ($\sim 1200 \text{ nm}$) because of the higher damping factor of Ni. The wavelength-dependent performances of 10Ni/ Al_2O_3 were evaluated with the irradiation of different light wavelength regions (Fig. 3b), with the results displayed in Fig. 3c and d. Apparently, the activities of 10Ni/ Al_2O_3 were all more or less enhanced with the introduction of light of various regions. Noticeably, with the irradiation of proper wavelength range of light ($400\text{--}500 \text{ nm}$), the activity of 10Ni/ Al_2O_3 could be 1.3 times improved even at the light intensity as low as 0.06 W cm^{-2} (Table S1). Controlled experiments indicated that the enhanced activity of 10Ni/ Al_2O_3 with light irradiation was not due to support Al_2O_3 (Table S2) nor the interaction between Ni and Al_2O_3 (Fig. S19). Then it could be speculated that the enhanced performance was related with the properties of Ni under light irradiation. By roughly assuming the center of the introduced light and calculating the number of photons and apparent quantum efficiency (AQE, Table S1), a wavelength-dependent performance was obtained (Fig. 3d), which follows the trend of Ni plasmonic absorption simulated by Mie theory. It suggested that probably it was plasmonic Ni that enhanced the performance of $\text{Ni}/\text{Al}_2\text{O}_3$ under light irradiation. The reason for the high AQE values (AQE as high as 19.0% was obtained over 10Ni/ Al_2O_3 with the introduction of light in the range of $400\text{--}500 \text{ nm}$) will be discussed later.

3.4. Electromagnetic field simulation

To further confirm the speculation, the intensity of the electromagnetic field over the $\text{Ni}/\text{Al}_2\text{O}_3$ catalysts, which served as an indicator of the intensity of Ni LSPR, was simulated via the finite-difference time-domain (FDTD) method (using numerical solver: FullWAVE, Synopsys' Rsoft), and the average sizes of Ni particles and the distances between two adjacent Ni particles (Table 1 and Fig. S3) were taken into consideration to establish the model for simulation. The simulated UV-vis spectrum (Figs. S20 and S21) matches with the one in Fig. 3a, implying the model works well. From Fig. 4, it's clear that there were enhanced electromagnetic fields over all the $\text{Ni}/\text{Al}_2\text{O}_3$ catalysts with the irradiation of monochromatic light (450 nm) which fell into the plasmonic band of Ni particles (Fig. 3a). The electromagnetic field enhancement was in the order of $10\text{Ni}/\text{Al}_2\text{O}_3 (21.7) > 5\text{Ni}/\text{Al}_2\text{O}_3 (14.8) > 15\text{Ni}/\text{Al}_2\text{O}_3 (11.8) > 20\text{Ni}/\text{Al}_2\text{O}_3 (8.3)$, consistent with the order of increment slope of the $\text{Ni}/\text{Al}_2\text{O}_3$ catalysts with light

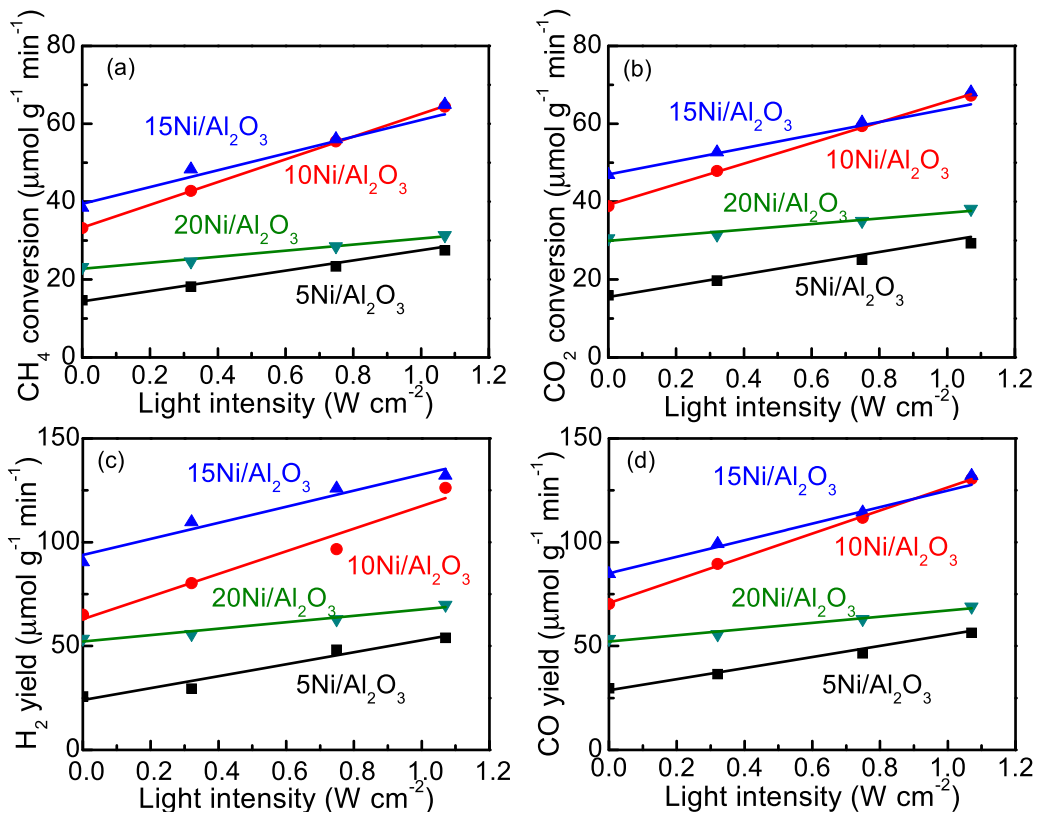


Fig. 2. Catalytic performances of the Ni/Al₂O₃ catalysts in DRM reaction at different light intensities. (a) CH₄ conversion, (b) CO₂ conversion, (c) H₂ yield and (d) CO yield. Reaction conditions: 550 °C, CH₄/CO₂ = 1, flowrate 20.0 mL/min, 0.050 g catalyst, light 300 nm < λ < 800 nm.

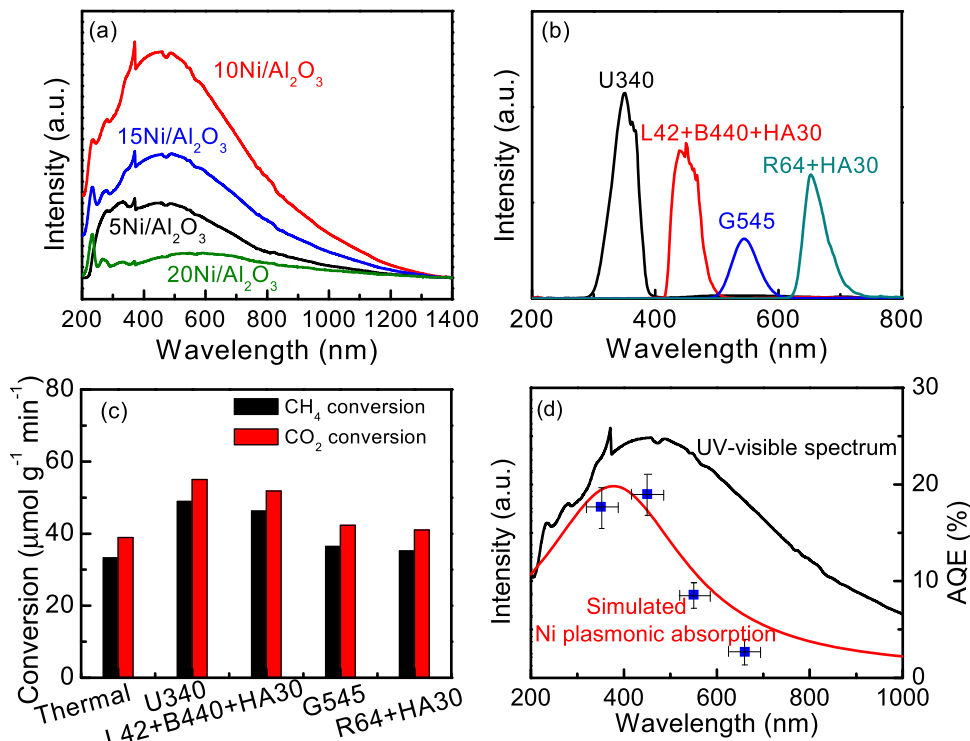


Fig. 3. (a) UV-vis spectra of the Ni/Al₂O₃ catalysts. (b) spectra of the light source obtained with different filter sets. (c) catalytic activities and (d) UV-vis spectrum, simulated plasmonic absorption of Ni particles by Mie theory and AQE values over 10Ni/Al₂O₃ without or with light of different range irradiation. Reaction conditions: 550 °C, CH₄/CO₂ = 1, flowrate 20.0 mL/min, 0.050 g catalyst, light 300 nm < λ < 800 nm.

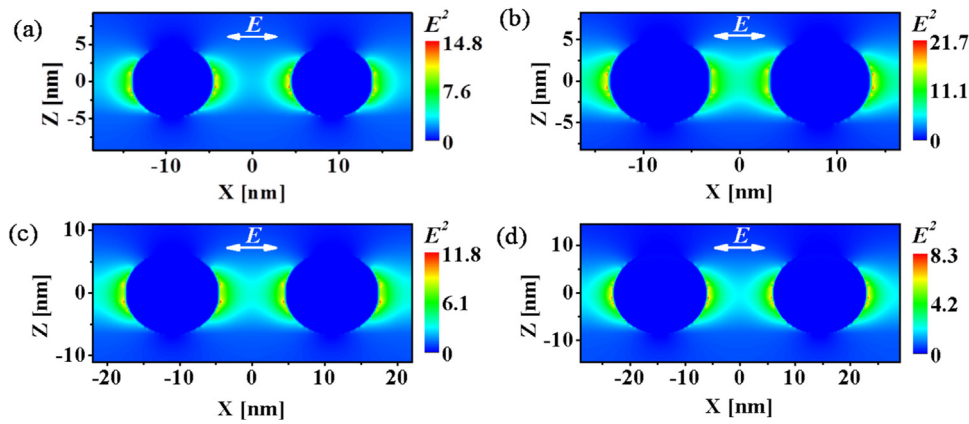


Fig. 4. Cross-sectional views of the electromagnetic field distribution and enhancement simulated with FDTD method (the color scale bar shows the electromagnetic field enhancement). (a) 5Ni/Al₂O₃, (b) 10Ni/Al₂O₃, (c) 15Ni/Al₂O₃, and (d) 20Ni/Al₂O₃.

irradiation within detection error (Fig. 2). Together with the wavelength dependent performance of 10Ni/Al₂O₃ in DRM (Fig. 3d), it could be speculated that it was plasmonic Ni that enhanced the performances of Ni/Al₂O₃ with light irradiation.

3.5. Mechanism study

The mechanism of Ni/Al₂O₃ catalysts in DRM with light irradiation was proposed. Considering the previous report that the hot electrons generated by Au LSPR could activate nonpolar molecules CO₂ and CH₄ and ultimately resulted in improved catalytic activity [19], then in this case, the hot electrons generated by Ni LSPR was suggested to also possess the ability to activate the reactants CH₄ and CO₂ with thermal assistance, although Ni possesses higher damping factor than noble metals such as gold or silver [24–27]. However, instead of the activation of CH₄ and CO₂ (Eqs. (1) and (2)), the reaction between the two adsorbed intermediates CH_x* and O^{*} (Eq. (3), * and ** represent the active sites for the activation of CH₄ and CO₂) was generally regarded as the rate determining step over Ni/Al₂O₃ catalysts [30–32], and the relatively far distances between two adjacent CH_x* and O^{*} species presented an obstacle and hindered the reaction rate within a limited level (Fig. 2) [30–32]. Then figuring out the pathway for Ni LSPR in enhancing the catalytic performances is of critical importance. The improved activities of Ni/Al₂O₃ catalysts with extra light irradiation gave evidences that Ni LSPR facilitated the rate determining step and accelerated the reaction between CH_x* and O^{*}. From this aspect, it is reasonable to assume that it's the intermediates of CO₂ and CH₄ activated by Ni LSPR that played the key roles.

Roughly speaking, there were three kinds of intermediate states, including adsorbed species [40,41], unadsorbed molecules [42] and free radicals [43–45]. The possibility of CH₄ and CO₂ activated by Ni LSPR via the adsorbed species could be excluded firstly, since there have been excessive adsorbed CH_x* and O^{*} intermediates owing to the fast rate of CO₂ and CH₄ activation under the thermal-driven condition (Eqs. (1) and (2)). Also, it's impossible for the intermediates existing as unadsorbed molecules (Eq. (4)), due to the unreality in the formation of free O₂ under the highly reductive atmosphere [46]. The intermediates of CH₄ and CO₂ activated by Ni LSPR are more likely in the radical states with random movement [45]. In our previous research, it was found that metal LSPR exhibited an analogous character with plasma [19], along with the activation pathway of CH₄ and CO₂ by plasma [47–49], and then CH₄ and CO₂ were inferred to be activated by the radical method, as shown in Eqs. (5) and (6). In order to check whether CH₄ and CO₂ were activated via radical pathway by Ni LSPR, *in-situ* ESR characterization were carried out over bulk Ni under pure CO₂ (or CH₄) atmosphere.

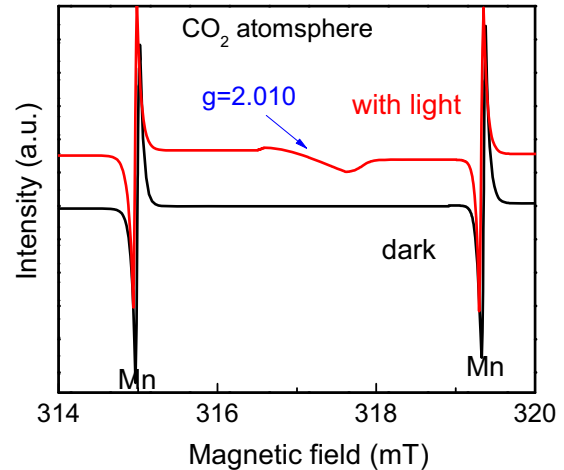
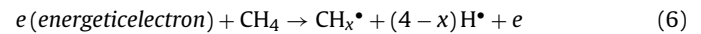
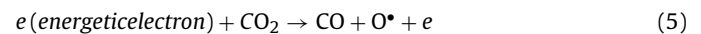
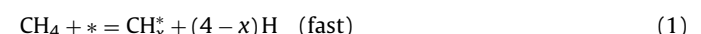


Fig. 5. *In-situ* ESR profiles of bulk Ni under dark condition and with light irradiation in CO₂ atmosphere (the two peaks at 315.0 and 319.3 mT were attributed to the reference Mn).

The results in Fig. 5 revealed the generation of oxygen radical at about 317.0 mT ($g = 2.010$) with light irradiation under pure CO₂ atmosphere, which supported the speculation that CO₂ was activated via the radical pathway even though the signal is quite weak. The reverse water gas shift reaction over Fe/SiO₂ catalyst also gave evidences on the CO₂ asymmetrical radical dissociation pathway (Fig. S22). On the contrary, the radicals generated by CH₄ could not be unlaboriously detected in the range of 330–350 mT (Fig. S23), probably due to that relatively high energy was required to activate CH₄¹⁶.



Then in this case, the enhanced performance of Ni/Al₂O₃ in DRM could be speculated. Hot electrons generated by Ni LSPR activate CO₂ via Eq. (5) to unadsorbed oxygen radical with free movement,

which accelerated the rate determining step through Eq. (7). More active sites were available for CH₄ activation by traditional thermal method with the gradual consumption of adsorbed CH_x^{*}. However, since the radicals generated via CH₄ activation by Ni LSPR were not detected (Eq. (6)), the contribution of Eq. (8) to the improved performance of Ni/Al₂O₃ with light irradiation could not be affirmed. The synergistic effects between photo-assistance and thermal-driven reaction lead to the relatively high AQE values.

3.6. Universality study

Except Ni, LSPR enhanced catalytic performance could also be observed over Fe- (Fig. S22), and Rh- (Fig. S24) based catalysts in light assisted CO₂ photoreduction; especially, the activity of Rh-based catalyst in DRM could be doubled via the excitation of Rh LSPR, which was close to the previously reported value on Rh-Au catalyst (Fig. S24) [19]. On the contrary, even with extra light irradiation, over Pt- (Fig. S14) and Pd- based (Fig. S15) catalysts, catalytic activities comparable to those evaluated under thermal-driven conditions were obtained. The non-enhanced performances over Pt-, Pd- based catalysts were probably due to that the sum- mit LSPR absorption of Pt [50] and Pd [51] were in deep ultraviolet region (220–260 nm), which were out of the wavelength range of the employed LA-251Xe lamp (Fig. S25).

4. Conclusions

In summary, Ni/Al₂O₃ catalysts with varied Ni loadings were prepared and employed in the reaction of CO₂ reforming of methane. With light irradiation, Ni served as both the active sites and the plasmonic promoter, interwoven the thermal-driven catalytic activity and the enhancement by Ni LSPR, the highest catalytic performance was obtained over 10Ni/Al₂O₃. With the irradiation of proper wavelength range of light (400–500 nm), the activity of 10Ni/Al₂O₃ could be 1.3 times enhanced even at the light intensity as low as 0.06 W cm⁻², and an AQE value of 19.0% was achieved. The LSPR enhanced catalytic performances could also be observed over other transition metals, such as Rh- and Fe- based catalysts. That is, universality on reactant activation by metal LSPR were expected, and most of the group VIII metals could also be adopted as plasmonic promoter and enhance the activity of a catalyst with light assistance. Additionally, the reactant activation behaviour by metal LSPR was also investigated, to be the radical dissociation pathway. This work provides guidance for the researches on adopting group VIII metals in photocatalytic reactions.

Acknowledgement

This work received financial support from the World Premier International Research Center Initiative (WPI Initiative) on Materials Nano-architectonics (MANA), MEXT (Japan), the National Basic Research Program of China (973 Program, 2014CB239301) and the National Natural Science Foundation of China (21633004).

Appendix A. Supplementary data

Supplementary data associated with this article can be found, in the online version, at <http://dx.doi.org/10.1016/j.apcatb.2017.02.080>.

References

- [1] D. Pakhare, J. Spivey, A review of dry (CO₂) reforming of methane over noble metal catalysts, *Chem. Soc. Rev.* 43 (2014) 7813–7837.
- [2] X. Meng, T. Wang, L. Liu, S. Ouyang, P. Li, H. Hu, T. Kako, H. Iwai, A. Tanaka, J. Ye, Photothermal conversion of CO₂ into CH₄ with H₂ over group VIII nanocatalysts: an alternative approach for solar fuel production, *Angew. Chem. Int. Ed.* 53 (2014) 11478–11482.
- [3] M. Anpo, H. Yamashita, Y. Ichihashi, Y. Fujii, M. Honda, Photocatalytic reduction of CO₂ with H₂O on titanium oxides anchored within micropores of zeolites: effects of the structure of the active sites and the addition of Pt, *J. Phys. Chem. B* 101 (1997) 2632–2636.
- [4] Z. Xu, Y. Lin, M. Yin, H. Zhang, C. Cheng, L. Lu, X. Xue, H. Fan, X. Chen, D. Li, Nanotubes: understanding the enhancement mechanisms of surface plasmon-mediated photoelectrochemical electrodes: a case study on Au nanoparticle decorated TiO₂ nanotubes, *Adv. Mater. Interfaces* 2 (2015) 1500169.
- [5] Y. Zhao, B. Zhao, J. Liu, G. Chen, R. Gao, S. Yao, M. Li, Q. Zhang, L. Gu, J. Xie, X. Wen, L. Wu, C. Tung, D. Ma, T. Zhang, Oxide-modified nickel photocatalysts for the production of hydrocarbons in visible light, *Angew. Chem. Int. Ed.* 55 (2016) 4215–4219.
- [6] Y. Zhao, G. Chen, T. Bian, C. Zhou, G.I.N. Waterhouse, L. Wu, C. Tung, L.J. Smith, D. O'Hare, T. Zhang, Defect-rich ultrathin ZnAl-layered double hydroxide nanosheets for efficient photoreduction of CO₂ to CO with water, *Adv. Mater.* 27 (2015) 7824–7831.
- [7] Y. Zhao, X. Jia, G.I.N. Waterhouse, L. Wu, C. Tung, D. O'Hare, T. Zhang, *Adv. Energy Mater.* 6 (2016) 1501974.
- [8] H. Yu, R. Shi, Y. Zhao, G.I.N. Waterhouse, L. Wu, C. Tung, Tierui Zhang, Smart utilization of carbon dots in semiconductor photocatalysis, *Adv. Mater.* 28 (2016) 9454–9477.
- [9] H. Tong, S. Ouyang, Y. Bi, N. Umezawa, M. Oshikiri, J. Ye, Nano-photocatalytic materials: possibilities and challenges, *Adv. Mater.* 24 (2012) 229–251.
- [10] R. Shi, T. Xu, L. Yan, Y. Zhu, J. Zhou, A visible-light-driven photocatalysts of Bi₂Mo₃S₂O₄ nanoplates with high energy efficiency and high activity, *Catal. Sci. Technol.* 3 (2013) 1757–1764.
- [11] M. García-Díéguez, I.S. Pieta, M.C. Herrera, M.A. Larrubia, L.J. Alemany, Nanostructured Pt- and Ni-based catalysts for CO₂-reforming of methane, *J. Catal.* 270 (2010) 136–145.
- [12] S.M. Stagg-Williams, F.B. Noronha, G. Fendley, D.E. Resasco, CO₂ reforming of CH₄ over Pt/ZrO₂ catalysts promoted with La and Ce oxides, *J. Catal.* 194 (2000) 240–249.
- [13] S. Linic, P. Christopher, D.B. Ingram, Plasmonic-metal nanostructures for efficient conversion of solar to chemical energy, *Nat. Mater.* 10 (2011) 911–921.
- [14] P. Christopher, H. Xin, S. Linic, Visible-light-enhanced catalytic oxidation reactions on plasmonic silver nanostructures, *Nat. Chem.* 3 (2011) 467–472.
- [15] A. Marimuthu, J. Zhang, S. Linic, Tuning selectivity in propylene epoxidation by plasmon mediated photo-switching of Cu oxidation state, *Science* 339 (2013) 1590–1593.
- [16] S. Sarina, H. Zhu, Q. Xiao, E. Jaatinen, J. Jia, Y. Huang, Z. Zheng, H. Wu, Viable photocatalysts under solar-spectrum irradiation: nonplasmonic metal nanoparticles, *Angew. Chem. Int. Ed.* 53 (2014) 2935–2940.
- [17] M.J. Kale, T. Avanesian, H. Xin, J. Yan, P. Christopher, Controlling catalytic selectivity on metal nanoparticles by direct photoexcitation of adsorbate-metal bonds, *Nano Lett.* 14 (2014) 5405–5412.
- [18] I.P. Silverwood, N.G. Hamilton, A.R. McFarlane, J. Kapitan, L. Hecht, E.L. Norris, R.M. Ormerod, C.D. Frost, S.F. Parker, D. Lennon, Application of inelastic neutron scattering to studies of CO₂ reforming of methane over alumina-supported nickel and gold-doped nickel catalysts, *Phys. Chem. Chem. Phys.* 14 (2012) 15214–15225.
- [19] H. Liu, X. Meng, T.D. Dao, H. Zhang, P. Li, K. Chang, T. Wang, M. Li, T. Nagao, J. Ye, CO₂ conversion through methane reforming under visible light: surface plasmon mediated nonpolar molecule activation, *Angew. Chem. Int. Ed.* 54 (2015) 11545–11549.
- [20] J. Wei, E. Iglesias, Isotopic and kinetic assessment of the mechanism of reactions of CH₄ with CO₂ or H₂O to form synthesis gas and carbon on nickel catalysts, *J. Catal.* 224 (2004) 370–383.
- [21] Y. Wang, H. Liu, B. Xu, Durable Ni/MgO catalysts for CO₂ reforming of methane: activity and metal-support interaction, *J. Mol. Catal. A: Chem.* 299 (2009) 44–52.
- [22] H. Liu, Y. Li, H. Wu, H. Takayama, T. Miyake, D. He, Effects of beta-cyclodextrin modification on properties of Ni/SBA-15 and its catalytic performance in carbon dioxide reforming of methane, *Catal. Commun.* 28 (2012) 168–173.
- [23] H. Liu, M. Li, T.D. Dao, Y. Liu, W. Zhou, L. Liu, X. Meng, T. Nagao, J. Ye, Design of PdAu alloy plasmonic nanoparticles for improved catalytic performance in CO₂ reduction with visible light irradiation, *Nano Energy* 26 (2016) 398–404.
- [24] Y. Zhang, A. Dragan, C.D. Geddes, Broad wavelength range metal-enhanced fluorescence using nickel nanodeposits, *J. Phys. Chem. C* 113 (2009) 15811–15816.
- [25] J. Chen, P. Alberla, Z. Pirzadeh, P. Alonso-González, F. Huth, V. Bonanni, J. Akerman, J. Nogués, P. Vavassori, A. Dmitriev, J. Aizpurua, Plasmonic nickel nanoantennas, *Small* 7 (2011) 2341–2347.
- [26] E.T. Papaioannou, V. Kapaklis, E. Melander, B. Hjorvarsson, S.D. Pappas, P. Patoka, M. Giersig, P. Fumagalli, A. Garcia-Martin, G. Ctistis, Surface plasmons and magneto-optic activity in hexagonal Ni anti-dot arrays, *Opt. Express* 19 (2011) 23867–23877.
- [27] Z. Xiong, X. Chen, X. Wang, L. Peng, D. Yan, H. Lei, Y. Fu, J. Wu, Z. Li, X. An, W. Wu, Size dependence of plasmon absorption of Ni nanoparticles embedded in BaTiO₃/SrTiO₃ superlattices, *Appl. Surf. Sci.* 268 (2013) 524–528.
- [28] P. Du, R. Eisenberg, Catalysts made of earth-abundant elements (Co, Ni, Fe) for water splitting: recent progress and future challenges, *Energy Environ. Sci.* 5 (2012) 6012–6021.

- [29] B. Su, Z. Cao, Z. Shi, Exploration of earth-abundant transition metals (Fe, Co, and Ni) as catalysts in unreactive chemical bond activations, *Acc. Chem. Res.* 48 (2015) 886–896.
- [30] T. Osaki, T. Mori, Role of potassium in carbon-free CO₂ reforming of methane on K-promoted Ni/Al₂O₃ catalysts, *J. Catal.* 204 (2001) 89–97.
- [31] R.R. Davda, J.W. Shabaker, G.W. Huber, R.D. Cortright, J.A. Dumesic, Aqueous-phase reforming of ethylene glycol on silica-supported metal catalysts, *Appl. Catal. B: Environ.* 43 (2003) 13–26.
- [32] T. Osaki, H. Fukaya, T. Horiuchi, K. Suzuki, T. Mori, Isotope effect and rate-determining step of the CO₂-reforming of methane over supported Ni catalyst, *J. Catal.* 180 (1998) 106–109.
- [33] P.B. Johnson, R.W. Christy, Optical constants of the noble metals, *Phys. Rev. B: Solid State* 6 (1972) 4370–4379.
- [34] E.D. Palik, *Handbook of Optical Constants of Solids*, 3rd edition, Academic press, 1998.
- [35] B. Xu, J. Wei, Y. Yu, J. Li, Q. Zhu, Carbon dioxide reforming of methane over nanocomposite Ni/ZrO₂ catalysts, *Top. Catal.* 22 (2003) 77–85.
- [36] D. Liu, X.Y. Quek, W.N.E. Cheo, R. Lau, A. Borgna, Y. Yang, MCM-41 supported nickel-based bimetallic catalysts with superior stability during carbon dioxide reforming of methane: effect of strong metal-support interaction, *J. Catal.* 266 (2009) 380–390.
- [37] M.C.J. Bradford, M.A. Vannice, Catalytic reforming of methane with carbon dioxide over nickel catalysts, *Appl. Catal. A: Gen.* 142 (1996) 97–122.
- [38] A. Donazzi, A. Beretta, G. Groppi, P. Forzatti, Catalytic partial oxidation of methane over a 4% Rh/α-Al₂O₃ catalyst part II: role of CO₂ reforming, *J. Catal.* 255 (2008) 259–268.
- [39] P. Djinović, I.G.O. Črnivec, B. Erjavec, A. Pintar, Influence of active metal loading and oxygen mobility on coke-free dry reforming of Ni-Co bimetallic catalysts, *Appl. Catal. B: Environ.* 125 (2012) 259–270.
- [40] P.D. Nolan, B.R. Lutz, P.L. Tanaka, J.E. Davis, C.B. Mullins, Molecularly chemisorbed intermediates to oxygen adsorption on Pt(111): a molecular beam and electron energy-loss spectroscopy study, *J. Chem. Phys.* 111 (1999) 3696–3704.
- [41] G. Novell-Leruth, A. Valcárcel, J. Pérez-Ramírez, J.M. Ricart, Ammonia dehydrogenation over platinum-group metal surfaces. structure, stability, and reactivity of adsorbed NH_x species, *J. Phys. Chem. C* 111 (2007) 860–868.
- [42] M.E. Jacox, The spectroscopy of molecular reaction intermediates trapped in the solid rare gases, *Chem. Soc. Rev.* 31 (2002) 108–115.
- [43] R.E. Heikkila, G. Cohen, 6-Hydroxydopamine: evidence for superoxide radical as an oxidative intermediate, *Science* 181 (1973) 456–457.
- [44] P.E.M. Siegbahn, R.H. Crabtree, Manganese oxyl radical intermediates and O–O bond formation in photosynthetic oxygen evolution and a proposed role for the calcium cofactor in photosystem II, *J. Am. Chem. Soc.* 121 (1999) 117–127.
- [45] W. Hou, S.B. Cronin, A review of surface plasmon resonance-enhanced photocatalysis, *Adv. Funct. Mater.* 23 (2013) 1612–1619.
- [46] Z. Yang, V.R. Mouré, D.R. Dean, L.C. Seefeldt, Carbon dioxide reduction to methane and coupling with acetylene to form propylene catalyzed by remodeled nitrogenase, *Proc. Nat. Acad. Sci.* 107 (2012) 19644–19648.
- [47] C. Liu, R. Mallinson, L. Lobban, Nonoxidative methane conversion to acetylene over zeolite in a low temperature plasma, *J. Catal.* 179 (1998) 326–334.
- [48] A. Oumghar, J.C. Legrand, A.M. Diamiy, N. Turillon, Methane conversion by an air microwave plasma, *Plasma Chem. Plasma Process.* 15 (1995) 87–107.
- [49] C. Liu, G. Xu, T. Wang, Non-thermal plasma approaches in CO₂ utilization, *Fuel Process. Technol.* 58 (1999) 119–134.
- [50] E. Gharibshahi, E. Saion, Influence of dose on particle size and optical properties of colloidal platinum nanoparticles, *Int. J. Mol. Sci.* 13 (2012) 14723–14741.
- [51] M.R. Knecht, M.G. Weir, A.I. Frenkel, R.M. Crooks, Structural rearrangement of bimetallic alloy PdAu nanoparticles within dendrimer templates to yield core/shell configurations, *Chem. Mater.* 20 (2008) 1019–1028.